A multiscale approach to model the anisotropic deformation of lithospheric plates

Mickael Knoll, Andrea Tommasi, Roland E. Logé, Javier W. Signorelli

Geochemistry Geophysics Geosystems G3
AN ELECTRONIC JOURNAL OF THE EARTH SCIENCES
Published by AGU and the Geochemical Society

Article
Volume 10, Number 8
14 August 2009
Q08009, doi:10.1029/2009GC002423
ISSN: 1525-2027

A multiscale approach to model the anisotropic deformation of lithospheric plates

Mickaël Knoll
Géosciences Montpellier, Université de Montpellier 2, CNRS, Place E. Bataillon, cc.060, F-34095 Montpellier CEDEX 5, France (knoll@gm.univ-montp2.fr)

Also at Centre de Mise en Forme des Matériaux, UMR 7635, MINES ParisTech, CNRS, 1, rue Claude Daunesse, B.P.207, F-06904 Sophia Antipolis CEDEX, France

Andréa Tommasi
Géosciences Montpellier, Université de Montpellier 2, CNRS, Place E. Bataillon, cc.060, F-34095 Montpellier CEDEX 5, France (andrea.tommasi@gm.univ-montp2.fr)

Roland E. Logé
Centre de Mise en Forme des Matériaux, UMR 7635, MINES ParisTech, CNRS, 1, rue Claude Daunesse, B.P. 207, F-06904 Sophia Antipolis CEDEX, France (roland.loge@mines-paristech.fr)

Javier W. Signorelli
Instituto de Física de Rosario, CONICET, Universidad Nacional de Rosario, Boulevard 27 de Febrero 210bis, 2000 Rosario, Argentina (signorelli@ifir-conicet.gov.ar)

[1] The association of experimental data showing that the plastic deformation of olivine, the main constituent of the upper mantle, is highly anisotropic and the ubiquitous seismic anisotropy in the upper mantle, which indicates that olivine crystals show coherent orientations over scales of tens to hundreds of kilometers, implies that the long-term deformation in the upper mantle is anisotropic. We propose a multiscale approach, based on a combination of finite element and homogenization techniques, to model the deformation of a lithospheric plate while fully considering the mechanical anisotropy stemming from a strain-induced orientation of olivine crystals in the mantle. This multiscale model explicitly takes into account the evolution of crystal preferred orientations (CPO) of olivine and of the mechanical anisotropy during the deformation. We performed a series of numerical experiments simulating the uniaxial extension of a homogeneous (100% olivine) but anisotropic plate to test the role of the olivine CPO on the plate mechanical behavior and the link between CPO and mechanical anisotropy evolution. Even for this simple solicitation, different orientations and intensity of the initial olivine CPO result in variable plate strengths and deformation regimes. A plate with an initial CPO where the olivine [100] and [010] axes are concentrated at 45° to the extension direction has high resolved shear stresses on the easy (010)[100] and (001)[100] slip systems of olivine. This results in low strength and in deformation by transtension. Plates with an initial CPO where the maximum of [100] axes is parallel or normal to the extension direction show a high initial strength. Isotropic plates have an intermediate behavior. The progressive rotation of olivine [100] axes toward the imposed stretching direction results in hardening in all models, except in those characterized by an initial concentration of olivine [100] axes normal to the imposed extension, in which softening is followed by hardening.

Components: 9020 words, 6 figures, 2 tables.

Keywords: anisotropy; olivine; viscous deformation; dislocation creep; crystal preferred orientations; structural inheritance.

Index Terms: 8032 Structural Geology: Rheology: general (8160); 8033 Structural Geology: Rheology: mantle (8162); 8031 Structural Geology: Rheology: crust and lithosphere (8159).

Received 6 February 2009; **Revised** 3 June 2009; **Accepted** 19 June 2009; **Published** 14 August 2009.

Knoll, M., A. Tommasi, R. E. Logé, and J. W. Signorelli (2009), A multiscale approach to model the anisotropic deformation of lithospheric plates, *Geochem. Geophys. Geosyst.*, *10*, Q08009, doi:10.1029/2009GC002423.

1. Introduction

[2] Most natural solids are polycrystalline, which means that they are made up of individual crystals that are defined by a shape, a size, and the orientation of the crystalline lattice. The presence of crystal preferred orientations (CPO) often induces a dependence of the physical properties on the direction of solicitation. This phenomenon is known as anisotropy. For simple solicitations, such as uniaxial extension or compression, this CPO-induced mechanical anisotropy results in a variation in the strains in the plane normal to the direction of the solicitation and it is usually characterized by the ratio between the maximum and minimum strain or r value. When the material is orthotropic (invariance of the deformation by three orthogonal planes) or transverse isotropic (invariance of the deformation by rotation around an axis), the r value fully defines its anisotropy. An anisotropic rheology may also result in development of shear strains during uniaxial compression or tension experiments and may therefore be characterized by the ratio of the shear strain relatively to the macroscopic equivalent strain. This parameter describes the tendency of anisotropic materials to develop ''out-of-plane'' strain components, which result in nonparallelism between principal stress and strain rate axes.

[3] Mechanical anisotropy has been extensively investigated in metallurgy. In metal forming or crash simulations, dealing with mechanical anisotropy during calculation is fundamental to predict the final material shape, the evolution of mechanical properties during deformation, damage distribution and failure. For instance, deep drawing of aluminum alloy sheets results in undesirable ''earing'' due to lower strengths and hence higher strain rates along ⟨110⟩ crystallographic directions [*Tucker*, 1961]. Numerous strategies have been developed to account for anisotropy during simulations of forming processes. Initial efforts focused on empirical description of yield surfaces based on a generalization of the Von Mises criterion [*Von Mises*, 1913] that was originally designed to approximate the plastic anisotropy of single crystals: the anisotropy coefficient [*Hill*, 1948]. However, this formulation is only valid for orthotropic materials to which is imposed a stress coaxial to a symmetry axis. Expressions for more complex strain rate states have been developed, but they are still limited to materials with an orthotropic initial texture [*Kim et al.*, 2007]. Coupling an empirical description of the yield surface to a finite element model (FEM) is straightforward, but the necessary parameters, in particular the dependence of the shape of the yield surface on the strain are difficult to obtain. This strategy also does not allow a description of the anisotropy for large deformations, because it does not account for the evolution of the crystallographic texture. An alternative approach consists of the parameterization of the texture and anisotropy evolution during deformation based on single crystal plasticity models. The *Ning and Aifantis* [1996] method, for instance, uses a distribution function of the CPO to define a texture tensor, which is used to model complex loadings on stainless steel. However, this approach is not suitable for modeling the deformation of orthorhombic or even lower symmetry materials, because no simple parameterization of the anisotropy evolution can be obtained.

[4] For nonorthotropic materials, the mechanical anisotropy has to be described via an analytical expression of the yield surface derived from a polycrystal plasticity model. A polycrystalline aggregate is associated to each integration point of the FEM and a homogenization method is used to link the mechanical states of the crystal to that of the polycrystalline aggregate [*Dawson et al.*, 2003]. The mechanical state of each grain is calculated by a single-crystal plasticity model and, using a given homogenization method, transmitted to the polycrystal. The repetition of this micro-macro calculation at all integration points of the FEM

allows describing the mechanical behavior in the FEM model as a function of the local CPO. This method gives good results in terms of evolution of the CPO and of the induced anisotropy during the deformation process and allows the study of plastic anisotropy independently of the symmetry of the material, but computation times are important. Different methods have been proposed recently to enhance computation times. *Zhao et al.* [2001] and *Raabe et al.* [2002] propose the use of texture components, i.e., a small set of discrete and mathematically compact Gaussian texture components, to map the orientation distribution. *Béringhier et al.* [2007] proposed to distribute the initial CPO over several elements of the FEM. Finally, *Gillet-Chaulet et al.* [2005] developed a micro-macro model for describing the behavior of anisotropic ice assuming it flows as a linearly viscous orthotropic material. The flow law is defined by six parameters and its orthotropic fabric described by an orientation distribution function depending on two parameters, the grain c axis colatitude and longitude. This model remains nevertheless limited to transverse isotropic materials.

[5] Most minerals, because of their lower symmetry, display a much higher plastic anisotropy than metals. A few early works investigated the role of an anisotropic viscosity on the convection geometry. By using a simplified description of the viscosity tensor, where the anisotropy is expressed as a constant ratio between normal and shear viscosities, these studies concluded that the effect of mechanical anisotropy was minor [*Christensen*, 1987; *Honda*, 1986; *Richter and Daly*, 1978]. Most studies in the last 25 years [*Blackman et al.*, 1993; *Chastel et al.*, 1993; *Kaminski and Ribe*, 2001, 2002; *Ribe*, 1989; *Tommasi*, 1998] focused therefore on the relation between olivine CPO and the seismic anisotropy in the upper mantle, neglecting the role of CPO-induced mechanical anisotropy on the viscoplastic, dislocation creep controlled, deformation of the Earth's interior. A series of recent studies suggest nevertheless that an anisotropic viscosity in the mantle may significantly modify its deformation. Models that use a similar description of the viscosity as the early ones, but consider that the anisotropy evolves as a function of the strain, suggest that a CPO-induced mechanical anisotropy does affect the development of convective instabilities [*Lev and Hager*, 2008; *Muhlhaus et al.*, 2004]. Models using an analytical description of anisotropic viscosity that decomposes the viscosity tensor in an isotropic part and an anisotropic part that depends of the geometry of the crystal predict that the flow of the transition zone in the Earth's mantle may be strongly affected by mechanical anisotropy [*Pouilloux et al.*, 2007]. However, all these models either use a highly simplified description of the anisotropy or are based on analytical developments that limit their application to high-symmetry materials. They cannot fully describe the mechanical anisotropy in the upper mantle that is mainly composed of orthorhombic olivine.

[6] Multiscale mechanical models similar to those developed in Material Sciences are thus necessary to fully account for an evolving anisotropic viscosity in the Earth's upper mantle. In the present study, we investigate the role of a CPO-induced mechanical anisotropy on the deformation of lithospheric plates by coupling a self-consistent polycrystal plasticity model to a finite element formulation using an updated Lagrangian framework. These models fully account for an anisotropic viscosity that evolves as a function of the olivine CPO and hence as a function of the local strain history. They can therefore be used to study the interplay between CPO evolution and anisotropic deformation in the lithospheric mantle. *Tommasi and Vauchez* [2001] already used viscoplastic self-consistent polycrystal plasticity models to study the reactivation of preexisting collisional structures during the continental rifting process. They showed that the mechanical anisotropy associated with preferred orientation of olivine crystals in the upper mantle may result in directional softening, leading to strain localization and shearing parallel to the preexisting tectonic fabric when the latter is oblique to the extensional stresses. However, these early models did not allow for the evolution of the CPO in response to an evolving stress field. They indicated the initial trend of the system, but did not predict its evolution.

[7] The physical properties of the olivine crystal in the upper mantle are presented in section 2. The multiscale modeling approach developed in the present work is detailed in section 3. Its application to the study of the extension of a homogeneous but anisotropic continental plate are presented in sections 4 and 5.

2. Anisotropy of Physical Properties in the Olivine Crystal and in the Upper Mantle

[8] Olivine is the major mineral in the upper mantle (50–80%). Its rheology is therefore crucial

for both the lithospheric deformation and the mantle convection. Olivine presents an orthorhombic crystallographic symmetry. Analysis of naturally deformed mantle samples from a large variety of geodynamic environments [*Ben Ismail and Mainprice*, 1998; *Le Roux et al.*, 2008; *Tommasi et al.*, 2000, 2004, 2008] and deformation experiments under a large range of temperatures and pressures [*Bystricky et al.*, 2000; *Couvy et al.*, 2004; *Raterron et al.*, 2007; *Zhang and Karato*, 1995] suggest that the upper mantle deforms mainly by dislocation creep. This mode of deformation depends strongly on the crystal structure. Dislocations move in well-defined slip systems characterized by a glide plane and direction – the Burgers vector. The ease of activation of a given slip system is given by the Critical Resolved Shear Stress (CRSS), whose magnitude depends on the crystal cell parameters and on the strength of the atomic bonds. Low-symmetry crystals, like orthorhombic olivine, are highly anisotropic because the total number of slip systems is reduced, while CRSS values vary considerably from one system to another. Compression experiments on olivine single crystals under high-temperature conditions show that strain rates vary by more than 2 orders of magnitude depending on the orientation of the crystal [*Bai et al.*, 1991; *Durham et al.*, 1977]. A direct consequence of this plastic anisotropy is the development of strong CPO during deformation by dislocation creep leading to an anisotropic mechanical behavior at the polycrystal (rock) scale.

[9] The elastic deformation and hence the propagation of seismic waves in olivine are also highly anisotropic [*Abramson et al.*, 1997]. Seismic anisotropy measurements based on the analysis of the splitting of core shear waves [*Silver and Chan*, 1986; *Vinnik et al.*, 1994] or of the variation of surface waves velocities as a function of the propagation (azimuthal anisotropy) or polarization directions [*Montagner and Nataf*, 1986] are the best tools available to map the mantle deformation. These measurements show that anisotropy is ubiquitous in the uppermost 200 km of the mantle [*Montagner*, 1998] (see also the shear wave splitting database available at http://www.gm.univ-montp2.fr/splitting). They also imply that olivine CPO are coherent over scales ranging from tens to hundreds of kilometers. This, together with the strong plastic anisotropy of olivine, suggests that the long-term mechanical behavior of the shallow mantle should be strongly anisotropic.

[10] Both the mechanical anisotropy and the CPO evolution depend strongly on the potential slip systems and on their critical resolved shear stresses (CRSS). However, CRSS are not absolute values; they depend on physical parameters such as temperature, pressure, or deviatoric stresses and on the chemical environment, in particular on the water and oxygen fugacity. Deformation experiments on olivine single crystals and aggregates, together with transmission electron microscopy observations on naturally and experimentally deformed peridotites show that deformation in the dislocation creep regime is essentially accommodated by glide on {0kl}[100] and {hk0}[001] systems, with (010), (001), and (100) being the most common glide planes. Slip on [100] systems is favored under high-temperature, low-stress, low-pressure and dry conditions [e.g., *Bai and Kohlstedt*, 1992; *Bai et al.*, 1991; *Darot and Gueguen*, 1981; *Doukhan et al.*, 1984; *Durham and Goetze*, 1977; *Durham et al.*, 1977; *Goetze and Kohlstedt*, 1973; *Mackwell et al.*, 1985; *Phakey et al.*, 1972; *Raleigh*, 1968], whereas high stress, high pressure, and high water contents favor [001] slip [*Couvy et al.*, 2004; *Jung et al.*, 2006; *Mainprice et al.*, 2005; *Raterron et al.*, 2007]. On the basis of these data, we propose that deformation in the lithospheric mantle is essentially accommodated by dislocation glide on {0kl}[100] systems. Olivine CPO measured in peridotite xenoliths and massifs that sample the upper 200 km of the mantle are indeed well reproduced by polycrystal plasticity simulations that use CRSS derived from high-temperature, low-stress deformation experiments on olivine single crystals [*Tommasi et al.*, 2000; *Wenk et al.*, 1991]. The same CRSS values (Table 1) are therefore used in the present simulations.

3. Multiscale Modeling of the Deformation of Anisotropic Low-Symmetry Polycrystalline Materials

[11] The deformation of an anisotropic polycrystalline material is modeled by a two-step scale transfer approach. The polycrystal mechanical behavior, characterized by an anisotropic viscosity tensor, is obtained from homogenization of the individual (representative) grains behavior, described by a standard single crystal plasticity model, using a viscoplastic self-consistent (VPSC) approach [*Lebensohn and Tomé*, 1993]. In contrast to the classical models of *Taylor* [1938] and *Sachs* [1928] that assume either homogeneous strain or

Table 1. Olivine Slip Systems and Associated Critical Resolved Shear Stresses and Stress Exponent Used in VPSC Calculations

Slip Systems	CRSS	Stress Exponent
(010)[100]	1	3
(001)[100]	1	3
(010)[001]	2	3
(100)[001]	3	3
{011}[100]	4	3
{111}[110]	50	3
{111}[011]	50	3

stresses in the sample, the VPSC model imposes both strain compatibility and stress continuity between grains and their environment. The latter is represented by a Homogeneous Equivalent Medium (HEM), which have the homogenized, calculated properties of the polycrystal.

[12] The VPSC approach considers each crystal as an inhomogeneity embedded in a HEM, in the sense of the Eshelby formalism [*Eshelby*, 1957]. At the crystal scale, deformation is accommodated by dislocation glide only. The shear rate induced in a slip system (s) is related to the local deviatoric stress **s** tensor by a nonlinear viscous response:

$$\dot{\gamma}^s = \dot{\gamma}_\circ \frac{\tau_r^s}{\tau_c^s}\left|\frac{\tau_r^s}{\tau_c^s}\right|^{n^s-1} = \dot{\gamma}_\circ \frac{m_{ij}^s s_{ij}}{\tau_c^s}\left|\frac{m_{ij}^s s_{ij}}{\tau_c^s}\right|^{n^s-1}, \quad (1)$$

where $\dot{\gamma}_\circ$, τ_r^s, τ_c^s, n^s, are a reference strain rate, the resolved shear stress on the system s, the CRSS, and the inverse of the rate sensitivity of the slip system s, respectively. $\mathbf{m}^s$ is the symmetric part of the Schmid orientation tensor of the system (s) defined by its normal to the glide plane **n** and the Burgers vector **b**:

$$m_{ij}^s = \frac{1}{2}\left(n_i^s b_j^s + n_j^s b_i^s\right) \quad (2)$$

The plastic strain rate $\dot{e}_{ij}$ in the crystal is the sum of the shear rate $\dot{\gamma}$ in all active systems:

$$\dot{e}_{ij} = \dot{\gamma}_\circ \sum_{s=1}^{\#sys} m_{ij}^s \frac{m_{pq}^s s_{pq}}{\tau_c^s}\left|\frac{m_{pq}^s s_{pq}}{\tau_c^s}\right|^{n^s-1} \quad (3)$$

The interaction between grains and the HEM is defined by

$$\begin{cases} \dot{e}_{ij} - \dot{E}_{ij} = -\alpha \tilde{M}_{ijkl}(s_{kl} - S_{kl}) \\ S_{ij} = \eta_{ijkl}\dot{E}_{kl} \end{cases} \quad (4)$$

where the microscopic strain rate tensor and the deviatoric stress tensor for each grain ($\dot{\mathbf{e}}$, **s**) and the equivalent macroscopic quantities ($\dot{\mathbf{E}}$, **S**) are linked by an interaction tensor $\tilde{\mathbf{M}}$ of fourth order. α is a scalar that allows tuning the strain compatibility and stress equilibrium constraints. Its effect on the olivine CPO evolution is shown by *Tommasi et al.* [2000]. In the present models, the standard tangent approach is used ($\alpha = 1$). The VPSC approach allows therefore calculating, for a given olivine CPO and an imposed velocity gradient, both the texture evolution and the full anisotropic macroscopic viscosity tensor $\boldsymbol{\eta}$. To maintain reasonable computation times, recrystallization or grain growth are not considered in the present models.

[13] The second step of the scale transfer consists of determining the effect of the local CPO-induced anisotropy on the large-scale stress and strain field. The large-scale deformation is modeled using an updated Lagrangian framework. In this incremental approach, the time is discretized such that the body is subjected to small strain increments during each time step $[t, t + \Delta t]$. At time t, the configuration of the body is known and the balance laws of the mechanical problem are solved in that configuration on the basis of stresses calculated at time $t + \Delta t$. The new configuration is then updated using an Euler explicit scheme as follows:

$$\mathbf{x}(t + \Delta t) = \mathbf{x}(t) + \mathbf{v}(t)\Delta t, \quad (5)$$

with **x** the node coordinate vector and **v** the velocity vector solution of the mechanical problem on the current configuration. In this context, the kinematics can be described using Eulerian variables, namely the velocity gradient tensor **L**:

$$\mathbf{L} = \nabla \mathbf{v} = \dot{\mathbf{E}} + \mathbf{W}, \quad (6)$$

where $\dot{\mathbf{E}}$ and **W** correspond, respectively, to the strain rate and the spin. The stress measure consistent with this approach is the Cauchy stress, in the limit of small strain increments over each time step.

[14] The finite element approach uses a mixed velocity/pressure formulation based on the separation of Cauchy stress tensor into its deviatoric and volumetric parts [*Chenot and Bay*, 1998]. The field equations governing the problem are the equilibrium and the continuity equations (volumetric response):

$$\begin{cases} div(\mathbf{S}) - \nabla p = 0 \\ div(\mathbf{v}) = 0, \end{cases} \quad (7)$$

with **S** and p the deviatoric and the pressure (volumetric) components of the Cauchy stress tensor.

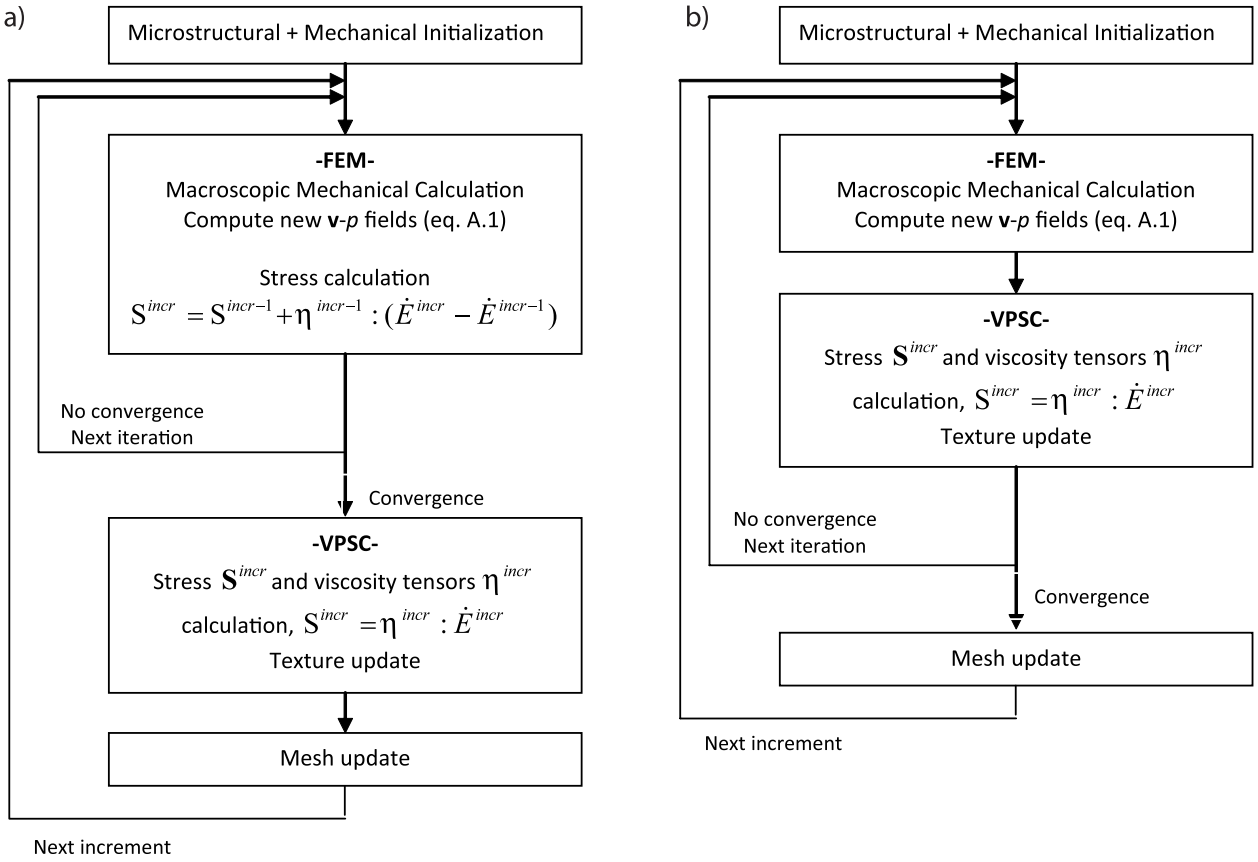

Figure 1. Flowchart of multiscale models with (a) a loose coupling strategy, where the VPSC model is called 1 time per increment, and (b) a strong coupling strategy, where the VPSC model is called n times per increment, with n being the number of iterations necessary to achieve convergence in the FEM iterative procedure.

[15] The coupling between the homogenization formalism and the FEM formulation is performed through a finite set of crystallographic orientations associated with the integration point of each mesh element. At each time increment, the calculated displacement rate (or velocity) gradient tensor in the FEM is used as the boundary condition for the VPSC simulation, allowing the calculation of the CPO evolution and of the anisotropic rheology. The viscosity tensor $\boldsymbol{\eta}$ obtained from the VPSC calculation and the local macroscopic strain rate tensor $\dot{\mathbf{E}}$ are then used to calculate the new stress $\mathbf{S}$:

$$S_{ij} = \eta_{ijkl}\dot{E}_{kl} \tag{8}$$

There are two ways of coupling the FEM and the VPSC models (Figure 1), i.e., using the VPSC macroscopic viscosity tensor to determine the FEM mechanical fields. The first is the strong coupling strategy, in which the polycrystal plasticity calculation is performed within the FEM iterative procedure. The stress tensor obtained after convergence is thus determined from an evolving estimate of the viscosity tensor (Figure 1b). The second strategy, known as the loose coupling approach, runs the polycrystalline calculation only at the end of the FEM time increment, after convergence. In this case, the FEM iterative procedure uses the viscosity tensor calculated at the previous time step to estimate the stresses (Figure 1a). The strong coupling strategy is very stable, but significantly slower. The stability of the loose coupling strategy is directly linked to the variability of rheological parameters within a time increment. In both strategies the convergence is verified independently at the two model scales (FEM and VPSC). Equilibrium and compatibility are ensured with a tolerance of 1% ($\|\langle \mathbf{s} \rangle - \mathbf{S}\| < 0.01$ and $\|\langle \dot{\mathbf{e}} \rangle - \dot{\mathbf{E}}\| < 0.01$) each time the VPSC model is called by the finite element solver. If convergence in either the VPSC calculation or the finite element solver is not achieved the simulation is stopped.

[16] A detailed study of the compression of textured polycrystalline Al volumes showed that loss of accuracy due to the use of a loose coupling strategy is negligible [*Logé and Chastel*, 2006]. However, most rock-forming minerals have a lower symmetry and hence a higher anisotropy compared to the FCC Al. To verify if the loose coupling strategy is applicable to low-symmetry materials, like olivine, we compare the results of simulations of 60% axial shortening parallel to the X direction of a cube of polycrystalline olivine discretized by 69 FE using both strong and loose coupling strategies (Figure 2a). To fully validate the coupled models, we also compare the texture evolution and mechanical behaviors predicted for these models to those predicted by a classical tangent VPSC model that is not coupled to a FEM. Since the coupled models simulate the behavior of a homogeneous material submitted to simple boundary conditions, their predictions should be similar to those of the classical uncoupled VPSC model. In these tests, an olivine polycrystal characterized by an initially random CPO defined by a set of 1000 orientations is associated to each Gauss point of the finite element mesh. Olivine slip systems, their CRSS and stress exponents are defined in Table 1.

[17] For similar conditions, strong coupling computation times (87 h) are >100 times higher than those for the loose coupling models (44 min). Final textures resulting from the two coupling strategies are very similar (Figure 2). As expected, they reproduce well those predicted by the classical, noncoupled VPSC approach for a single olivine polycrystal submitted to axial shortening [*Tommasi et al.*, 1999]. They display an axial symmetry relatively to the shortening direction (X direction), characterized by a concentration of [010] axes around it and a girdle distribution of [100] and [001] axes at high angle to it. Averages over all finite elements of the deviatoric strain rate tensor components normalized by the Von Mises equivalent strain rate, $\dot{E}_{eq} = \sqrt{\frac{2}{3}\left(\dot{E}_{ij}\,\dot{E}_{ij}\right)}$ obtained using the strong and loose coupling strategies are also compared to the macroscopic deviatoric strain rates predicted by the classical noncoupled VPSC calculation that uses both stress and strain rate boundaries conditions to evaluate the evolution of the strain rate tensor during the calculation (Table 2). For the diagonal components of the normalized deviatoric strain rate tensor ($\dot{E}_{ii}/\dot{E}_{eq}$ (i = 1,2,3)), the average difference between the 3 calculations does not exceed 0.86%. The average difference between normalized shear strain rate components ($\dot{E}_{ij}/\dot{E}_{eq}$ (i,j = 1,2,3, $i \neq j$)) predicted using the strong and loose coupling strategies does not exceed 8% except for a few elements close to the model boundaries. One should note however that nondiagonal components are 3–5 orders of magnitude smaller than the diagonal ones. The strain rate tensor remains consistent for all elements of the initial mesh, even when exceeding 60% deformation in compression. The loose coupling approach is therefore used in all following simulations.

4. Modeling the Deformation of a Homogeneous Anisotropic Lithospheric Plate

[18] All models were run using a plate of 1 × 1 × 0.1 adimensional units submitted to either a constant extensional stress or a constant extensional velocity parallel to X on the left boundary (Figure 3). Free slip conditions are applied to the opposed boundary, except for two nodes on its meridian line that are fixed in X and Y directions to avoid translation or body rotation of the plate. The remaining boundaries are free. The present study focuses on the deformation of an anisotropic viscous polycrystalline material. Elastic or thermal effects are not considered.

[19] A polycrystal composed of 1000 initially spherical olivine crystals is associated with each Gauss point of the FEM mesh. Olivine slip systems, their CRSS and stress exponents are defined in Table 1. In all models, the initial CPO is spatially homogeneous. Two different initial CPO were tested: a random quasi-isotropic initial olivine CPO (labeled Iso) and an orthorhombic CPO characterized by orthogonal maxima of [100], [010], and [001] (Figure 4). The latter CPO correspond to an olivine CPO pattern commonly observed in naturally and experimentally deformed mantle rocks [*Ben Ismail and Mainprice*, 1998]. Its intensity (concentration of the crystallographic axes), which may be quantified by the J index, that is the volume-averaged integral of the squared orientation densities [*Bunge*, 1992], is nevertheless significantly weaker (J = 3.3) than those of naturally deformed mantle rocks, whose J indexes cluster between 6 and 12 [*Tommasi et al.*, 2000]. Three different orientations of this initial nonrandom CPO relatively to the imposed extension were tested: the [100] maximum is either parallel (models labeled 0°), normal (90° models), or at 45° to the extension direction X. The maximum concentration of [001] is always vertical (Z direction).

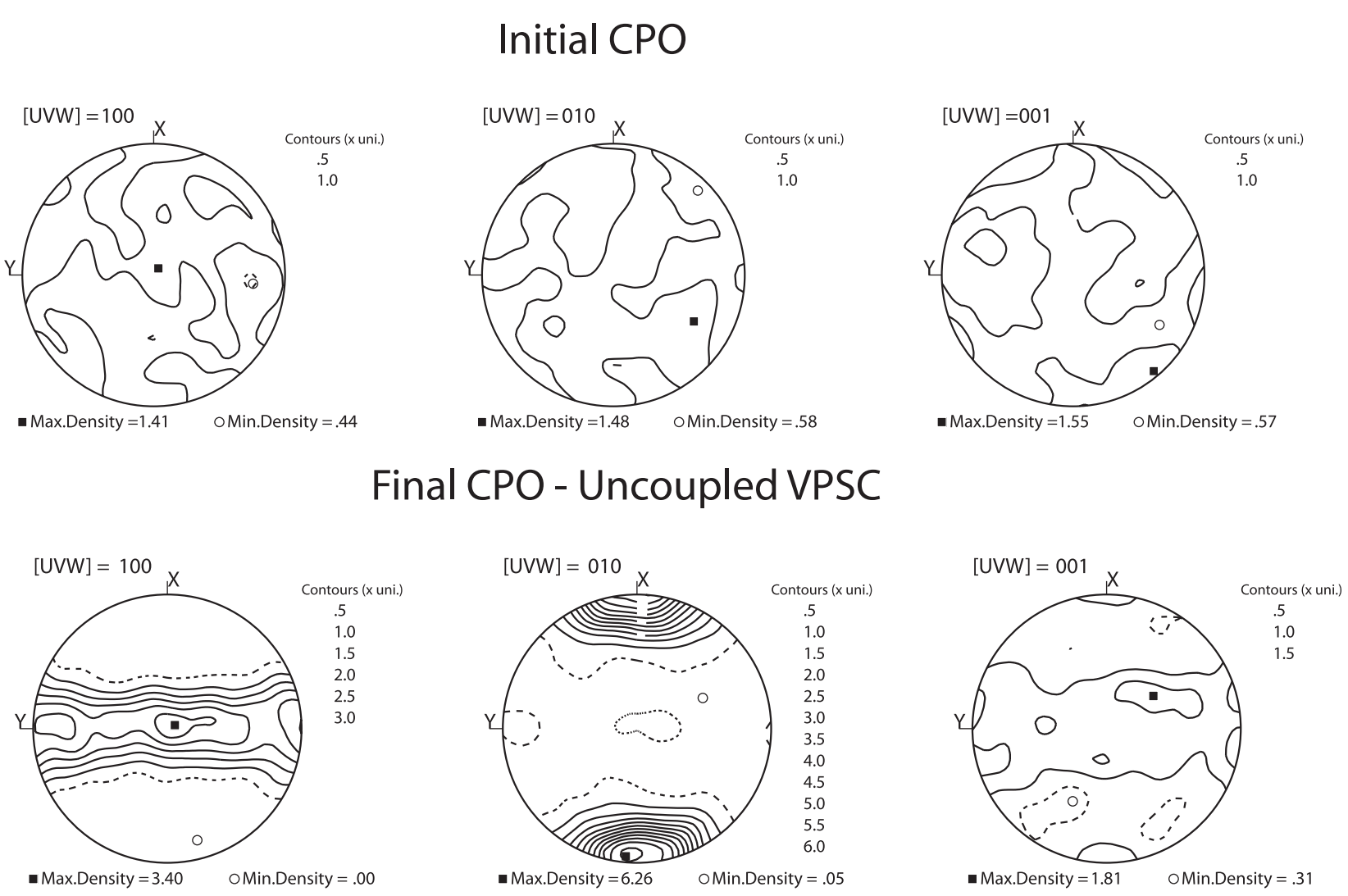

Figure 2. Validation test: initial random olivine CPO and CPO predicted after 60% axial shortening parallel to the X direction using the classical, noncoupled VPSC approach, as well as coupled models using the strong and loose coupling strategies.

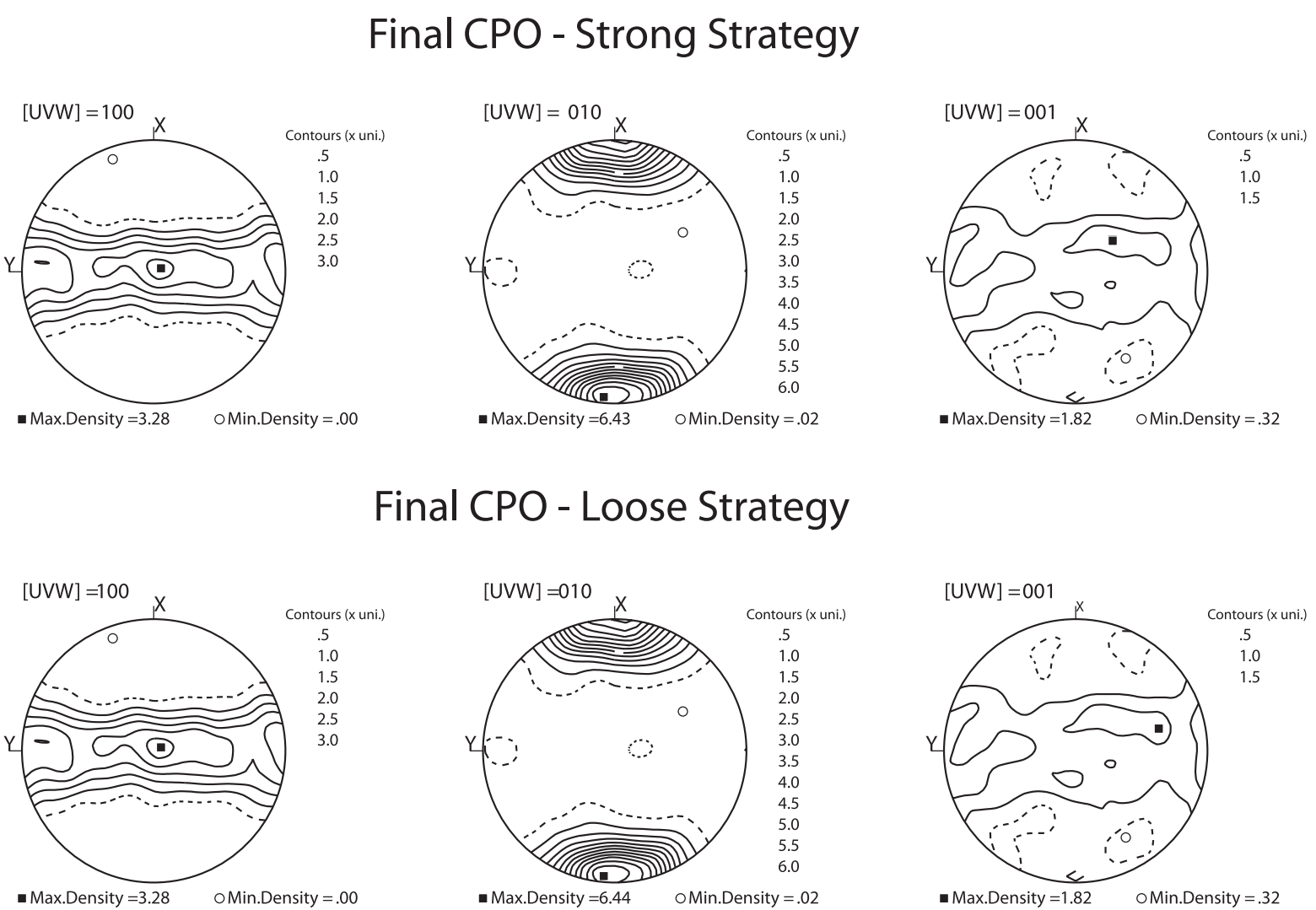

Figure 2. (continued)

Table 2. Averaged Normalized Strain Rates After 60% Axial Shortening in the X Direction for the Two Coupling Strategies and for the Traditional, Noncoupled Tangent VPSC Approach

	XX	YY	ZZ	XY	YZ	ZX
Loose strategy	−0.9946	0.4977	0.4969	0.0000	−0.0001	0.0011
Strong strategy	−0.9948	0.4983	0.4965	0.0000	−0.0006	0.0025
Uncoupled	−1.0000	0.5007	0.4993	0.0000	0.0000	0.0000

[20] All models were run for an adimensional time of 1. The effect of a CPO-induced anisotropy in viscosity is investigated by comparing the final macroscopic deformation (Figure 4) and the evolution of the extensional and shear strain rates normalized by the initial Von Mises equivalent strain rate for an isotropic medium $\dot{E}^{\circ}_{eq}$ and of the macroscopic anisotropy r value $r = \dot{E}_{zz}/\dot{E}_{yy}$ with increasing extensional strain in the different models (Figure 5). The interpretation of the variations in mechanical behavior is further constrained by the analysis of the evolution of the CPO in each model (Figure 4).

[21] The total macroscopic deformation, recorded by the final mesh shapes (Figure 4), in models in which a constant tensional stress of 1 parallel to the X direction is applied during a total adimensional time of 1, varies strongly as a function of the initial olivine CPO. The final macroscopic extension parallel to the X direction ranges from 21% in the 0° case, to 35% in the Iso case, 36% in the 45° case, and 48% in the 90° case. The final mesh geometry or strain regime also depends on the initial olivine CPO (Figure 4). While the Iso and 90° cases deform by pure extension in which stretching in the X direction is compensated by shortening in both Y and Z directions, the 45° case shows a transtensional deformation regime, in which extension parallel to X is associated with anticlockwise (sinistral) XY shearing. Deformation in the 0° case is also transtensional, but the extension/shearing ratio is higher than in the 45° case (lower vorticity).

[22] In all cases, the olivine CPO evolves with increasing strain. [100] axes tend to align in the extension direction, while [010] and [001] axes form variably developed girdles normal to it. The rate of change of the CPO depends strongly on the orientation of the CPO relatively to the imposed extension. Both 0° and 45° cases result in very strong olivine CPO, but in the latter an obliquity between the olivine CPO and the imposed extension persists even after 45% of extension. The 90° case shows a complex CPO evolution where fast reorientation of the main crystallographic axes is accompanied by slow concentration of the CPO.

[23] As a consequence of the CPO evolution, deformation regimes are not stationary, as shown by the variations of the deviatoric strain rate tensor

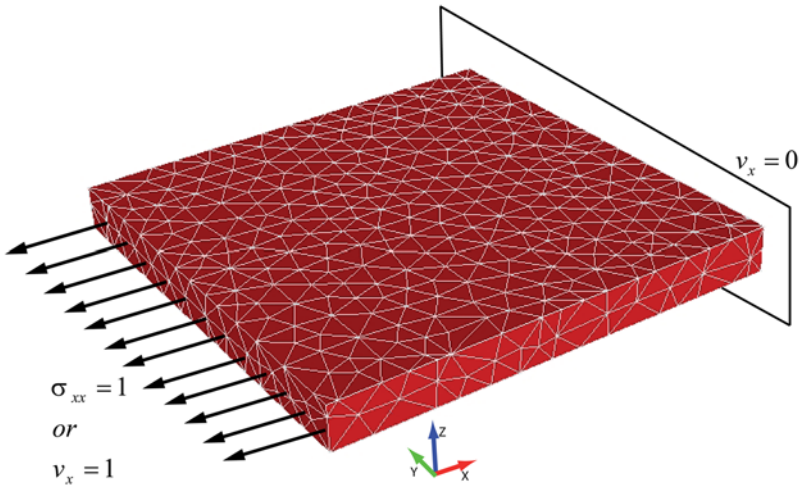

Figure 3. Initial mesh and boundary conditions for all models.

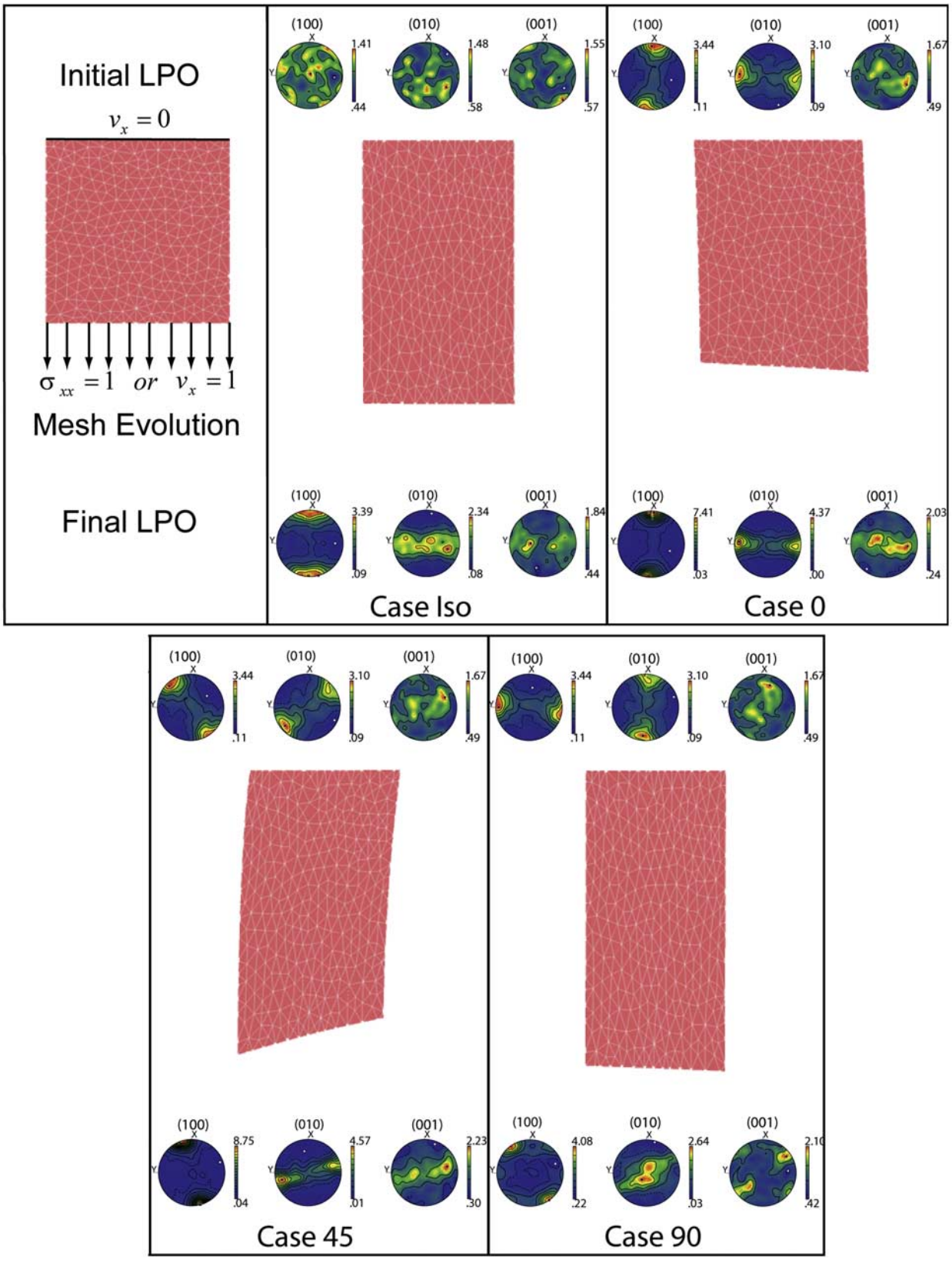

Figure 4. Macroscopic deformation (top view, XY plane) and evolution of olivine CPO in models where a homogeneous plate (100% olivine) with different initial CPO is submitted to a constant extensional stress parallel to X during an adimensional time of 1.

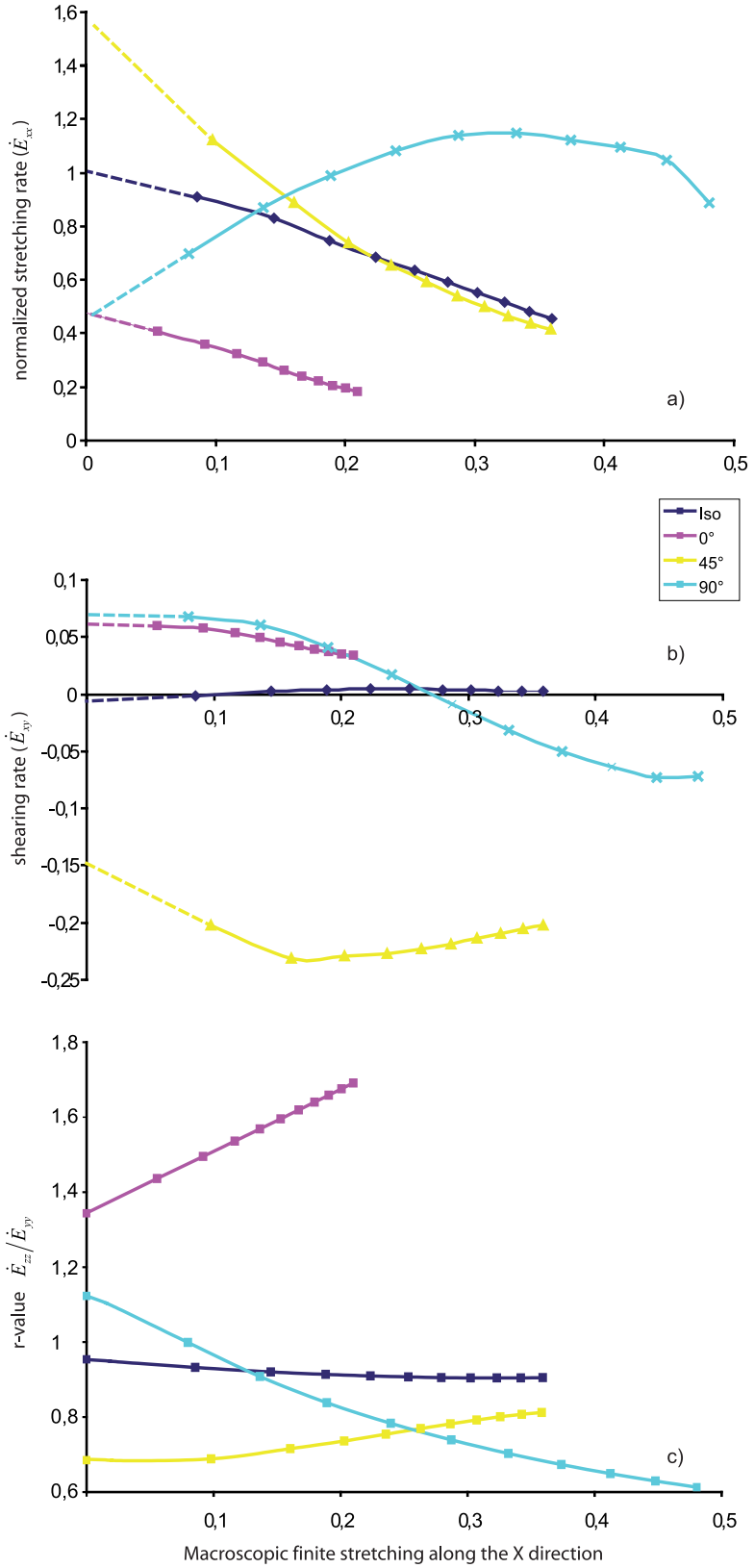

Figure 5. Evolution of (a) the normalized stretching rate ($\dot{E}_{xx}$), (b) the normalized shearing rate ($\dot{E}_{xy}$), and (c) the r value, $\dot{E}_{zz}/\dot{E}_{yy}$, as a function of the macroscopic finite stretching parallel to X for the Iso, 0°, 45°, and 90° models submitted to a constant velocity in the X direction during an adimensional time of 1. Values are plotted each 10 computation steps.

components (normalized by the initial Von Mises equivalent strain rate in an isotropic case) as a function of the macroscopic stretching along the X direction (Figure 5). In all models, deformation is essentially accommodated by stretching parallel to the *x* axis, in agreement with the imposed boundary conditions. Except for case Iso, which deforms by normal strains only, shear components in the horizontal plane ($\dot{E}_{xy}$) represent in average 1/10 of the extensional strain rates ($\dot{E}_{xx}$); the other shear components are one order of magnitude smaller than $\dot{E}_{xy}$. In the Iso case, CPO development results in hardening, recorded by a progressive decrease of the extensional strain rate with increasing strain. A similar behavior is observed in the 0° case, but the decrease in the extension rate is accompanied by an increase of the normalized shear strain rate due to a slight obliquity of the [100] maximum relative to the stretching direction. The 45° case also presents a monotonic evolution characterized by an increase of the normalized extension rate and a marked decline of the normalized shear rate. In contrast, the 90° case displays a complex evolution of the strain rate tensor. Up to 25% extension, the normalized stretching rate increases and the shear rate decreases. For extensions larger than 25%, the behavior is inversed; the stretching rate decreases and the shear rate increases, but the sense of shearing is inversed.

[24] The evolution of the r value allows to further characterize the effect of the CPO on the mechanical behavior of the plate. The Iso case is characterized by slightly faster shortening, giving an initial r value of 0.95 (the CPO is not completely isotropic) that slightly decreases with increasing strain. The observed deviation from isotropy outlines that 1000 random orientations are not enough to correctly describe an isotropic polycrystalline material. In the 45° case, shortening is initially significantly faster than thinning, but the evolution of the CPO with increasing strain results in a reduction of the anisotropy. In contrast, in the 0° case, thinning rates are higher than the shortening ones and this tendency is reinforced by the strengthening of the CPO with increasing strain; the r value increases by a factor of 1.3 during the calculation. Finally, the 90° case shows the strongest variation of the r value, expressing a change from dominant thinning to dominant shortening with increasing strain.

[25] To understand how the CPO influences the mechanical behavior of the plate, it is necessary to analyze the evolution of the olivine CPO with increasing strain in each model. In all four models (Figure 4), olivine [100] axes tend to align parallel to the imposed extension direction (X). This evolution expresses the influence of the imposed boundary conditions on the strain field and hence on the CPO development. However, the rate of CPO concentration and reorientation as well as the actual rotation path for the 3 principal crystallographic axes of olivine vary significantly from one case to another. The Iso case shows the typical CPO evolution for olivine polycrystals submitted to axial extension: [100], which is the Burgers vector for the 2 easy slip systems (Table 1), tends to align in the direction of the imposed extension, while [010] and [001] form a wide girdle normal to it, with a better organization of [010]. Concentration of the CPO with no reorientation is observed in the 0° case, because the initial orientation is already very close to the "equilibrium" orientation. In contrast, the 45° case is characterized by both a clockwise rotation of the CPO leading to a decrease of the angle between the maximum concentration of [100] and the extension direction (X) and a strengthening of the CPO. Finally, the 90° case presents a unique, two-stage CPO evolution (Figure 6). The first stage is characterized by a fast reorientation of the CPO, which aligns the maximum concentration of [010] in the Z direction, and by a slight decrease of the CPO strength. This dispersion of the CPO is probably due to strongly different behaviors of grains with initially similar orientations. Indeed, in this case, most grains were in hard orientations at the start of the simulation, because [010] is not an active Burgers vector in olivine and, hence, small variations in resolved shear stresses have a strong effect on the crystals mechanical behavior. This stage is then followed by a slow rotation of the [100] axes toward the imposed extension direction (X).

5. Discussion

[26] Analysis of the four simple models presented in this work shows that for low-symmetry materials, such as olivine and most rock-forming minerals, the orientation of the constituent crystals is a first-order parameter controlling the mechanical behavior of a polycrystal. Significantly different mechanical responses are observed as a function of the orientation of the initial olivine CPO relatively to the solicitation even for a homogeneous, 100% olivine plate submitted to simple boundary conditions.

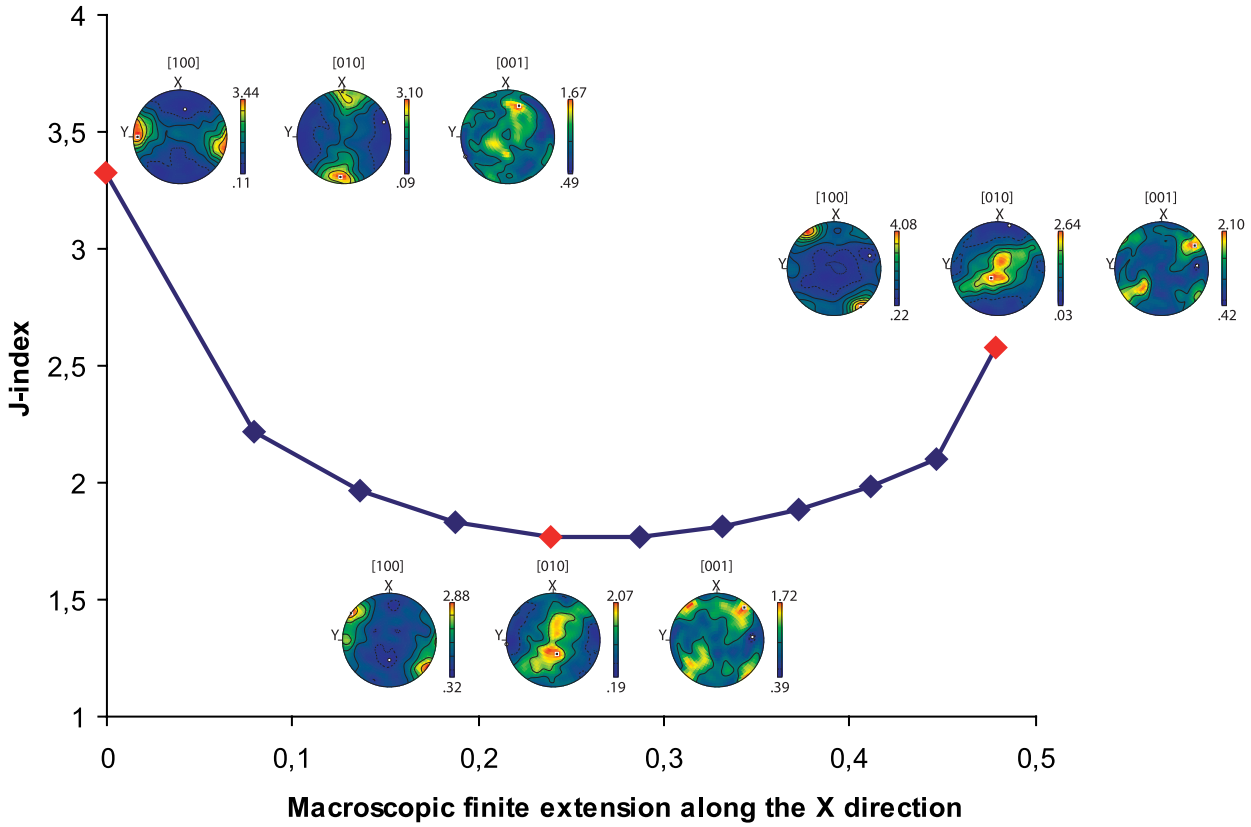

Figure 6. Textural evolution for the 90° case submitted to a constant extensional stress field during an adimensional time of 1.

[27] In the Iso case, the CPO develops in response to the applied extension; it is therefore symmetrically arranged relatively to the extension direction (Figure 4). In consequence, the sole expression of a CPO-induced anisotropic viscosity is a significant hardening, expressed by the decrease in strain rates with increasing strain. No shearing develops and shortening and thinning rates are similar. The observed hardening is essentially geometrical. The CPO evolution, characterized by a progressive rotation of the [100] axis of olivine crystals toward the extension direction, results in a decrease of the resolved shear stresses on the easy (010)[100] and (001)[100] slip systems (Table 1) and hence in a decrease of strain rate in the model with constant stress boundary conditions.

[28] The same mechanism results in a higher strength (or lower strain rates) in the 0° case relatively to the Iso model. With increasing strain, this CPO becomes more concentrated, without significant reorientation of the maxima, leading to further hardening. The orthorhombic symmetry of the initial olivine CPO induces a variation between the horizontal shortening and vertical thinning rates. Predominance of thinning, indicated by the observed positive r values, is coherent with the higher activation of the (001)[100] system relatively to the (010)[100] one (Figure 5). Finally, the slight asymmetry in the initial CPO (Figure 4) explains the development of dextral shearing (Figure 5).

[29] The effects of a CPO-induced anisotropic viscosity are even more marked in the 45° case. The strong obliquity of the initial CPO relatively to the imposed extension results in high resolved shear stresses on the easy (010)[100] and (001)[100] slip systems (Table 1) and hence in low strength of the plate. It also produces a strong sinistral (counterclockwise) shearing. However, the imposed extension leads to reorientation of the CPO. [100] progressively rotates toward the extension direction (X) and the [010] and [001] axes tend to form a girdle normal to it. This reorientation decreases the obliquity between the CPO and the imposed extension, leading to lower resolved shear stresses on the easy slip systems and hence to

progressive hardening of the plate, expressed by the decrease in strain rates with increasing strain (Figure 5). The reorientation of the CPO also leads to a decrease of the mechanical anisotropy (r value tends toward 1).

[30] Finally, the 90° case shows a complex textural evolution which results in a nonmonotonic evolution of the mechanical behavior of the plate. The initial rotation of the maximum concentration of [010] from the Y to the Z direction results in a change of the ratio between shortening and thinning rates, expressed by the variation of the r value (Figure 5). During this stage, the CPO intensity is slightly weakened and hence the plate strength decreases slightly. This is followed by a progressive rotation of the [100] axes toward the extension direction that results initially in geometrical weakening of the plate. This behavior will be inversed, leading to hardening, once the angle between the [100] concentration and the imposed stress direction becomes smaller than 45°. The observed shearing results essentially, as in the 0° case, from the departure from a perfect orthorhombic symmetry of the initial CPO.

[31] Even in the simple case analyzed here, that is, a homogeneous plate submitted to a constant extension normal to one of its boundaries, the variation in strength and deformation regimes for 4 different initial olivine CPO highlights the importance of accounting for an evolving CPO-induced anisotropy in geodynamical models. The present results outline that lateral contrasts in inherited olivine CPO in the lithospheric mantle of continental plates, which form by progressive accretion of terranes around ancient cratonic blocs during successive collision and rifting episodes [*Tommasi and Vauchez*, 2001; *Vauchez et al.*, 1998], should result in significant variations in the mechanical behavior of the plate, leading to strain localization in those domains for which the orientation of the inherited olivine CPO allows higher resolved shear stresses on the easy slip systems of the olivine crystals. The evolution of the system will depend on the imposed boundary conditions and on the initial CPO. The former controls, to the first order, the final, "ideal" CPO. However, the finite strain necessary to approach this "ideal" CPO depends on the initial texture (Figure 4). In extension, which is the case investigated in the present article, the progressive reorientation of the olivine [100] axes toward the main stretching direction results in hardening for all initial orientations. This suggests that the strength contrast will probably decay at large finite strains, leading to strain delocalization if other deformation mechanisms or thermal processes are not activated. However, as the hardening rates are strongly dependent on the initial CPO (Figure 5), strength contrasts may be maintained for significant times.

[32] Since the present model does not consider dynamic recrystallization, the CPO concentrates continuously, never reaching a stable configuration. Consequently, the anisotropy increases continuously, tending toward the single crystal mechanical behavior. In nature, however, processes like dynamic recrystallization allow stable CPO to be reached, buffering the mechanical anisotropy [*Tommasi et al.*, 2000]. Analysis of olivine polycrystals submitted to simple shear show that dynamic recrystallization accelerates the development of a stable CPO in an initially random aggregate [*Zhang and Karato*, 1995; *Bystricky et al.*, 2000]. This suggests that it may accelerate the decay of the strength contrasts. However, we lack experimental data on how dynamic recrystallization affects the CPO evolution in initially textured aggregates.

[33] Finally, the present models show that even a slight obliquity of the CPO relative to the solicitation direction results in development of significant shearing. Indeed, the 45° case, which has the strongest obliquity, deforms by an association of extension and shearing, i.e., in transtension. The present results confirm therefore the conclusions of previous studies that a CPO-induced mechanical anisotropy in the lithospheric mantle may explain the reactivation of preexisting lithospheric structures during rifting [*Tommasi and Vauchez*, 2001; *Vauchez et al.*, 1998]. They are also in agreement with the prediction by these studies that the reactivation of preexisting structures oblique to the extension direction should be characterized by a transtensional deformation, as observed, for instance, in the initial stages of the East Gondwana fragmentation [*Powell et al.*, 1988], and in the early stages of the East African rift and Rhine graben development [*Schumacher*, 2002; *Theunissen et al.*, 1996].

6. Conclusion

[34] Anisotropy of physical properties in polycrystalline materials, like rocks or, at a larger

scale, the Earth's mantle, is a fully multiscale problem. The ''polycrystal'' anisotropy depends on both the intrinsic anisotropy of the crystal and on the orientation of the crystals that compose this polycrystal. The present study shows that multiscale mechanical models, which couple a visco-plastic self-consistent (VPSC) description of the polycrystal plasticity to 3D finite element models that simulate the large-scale flow, allows to perform an accurate calculation of the extension of a mechanically anisotropic plate. The originality of this method is to use the VPSC approach to fully determine the viscosity tensor, on the basis of the local CPO and mechanical state, and, hence, to be able to account for its evolution during the deformation history. A major advantage of this method is that it is applicable to all crystalline materials, independent of their symmetry. The simple models presented here highlight that a CPO-induced anisotropy in viscosity in the mantle is a first-order parameter for the deformation of the plate, controlling not only the strain distribution, but also the deformation regimes. It may thus both contribute to strain localization in natural geological systems and explain the high proportion of shearing in these systems.

Appendix A: Finite Element Formulation

[35] The formulation of the finite element problem is based on the weak integral form of equation (7) with the appropriate boundary conditions:

$$\begin{cases} \int_\Omega \mathrm{S}(\mathrm{v}) : \dot{\mathrm{E}}(\mathrm{v}^*) d\Omega - \int_\Omega p \ tr\big(\dot{\mathrm{E}}(\mathrm{v}^*)\big) d\Omega - \int_{\partial\Omega} \mathrm{T}\cdot\mathrm{v}^* \ dS = 0 \qquad \forall \mathrm{v}^* \\ \int_\Omega p^* \ div(\mathrm{v}) d\Omega = 0 \qquad \forall p^* \end{cases}, \tag{A1}$$

with $\mathbf{v}^*$ and p^* any virtual velocity and pressure field defined over the configuration at time t. The finite element procedure leads to a global non-linear algebraic system of equations for the velocity field $\mathbf{v}$ and the pressure field p. The solution for a specified time interval is obtained incrementally by discretizing the time interval as mentioned in section 3. In each time step, the crystal constitutive equations are integrated at the local level and the solution of the global problem is obtained by a Newton-Raphson scheme. The solution procedure at a given time step t can be summarized as follows: (1) Calculate the initial estimate of the velocity vector (solution of the previous increment). (2) Compute the elemental velocity gradient used as the input to the constitutive model. (3) Integrate the constitutive law in order to compute state variables at time $t + \Delta t$ and the tangent modulus. (4) Solve the global system of equations for the new velocity and pressure fields using a Newton-Raphson algorithm until convergence is achieved. (5) If convergence occurs, update the velocity and pressure fields and the configuration of the body and move on to the next increment.

[36] The finite element spatial discretization is based on a linear isoparametric tetrahedron (P1 + /P1) where a bubble function is added at its center for the velocity field interpolation [*Chenot and Bay*, 1998]. The bubble function allows to satisfy the Brezzi/Babuska condition and enhances numerical stability [*Brezzi and Fortin*, 1991]. Since a linear interpolation is used, there is only one Gauss point per element for the integration of the constitutive equations.

Acknowledgments

[37] This study was partially funded by the program Action Marges of the Institut National des Sciences de l'Univers, Centre National de la Recherche Scientifique (INSU-CNRS), France. Collaboration with J.S. was supported by a CNRS-CONICET cooperation program. M.K. benefited of a Ph.D. scholarship from the Ministère de la Recherche et de l'Enseignement Supérieur, France.

References

Abramson, E. H., J. M. Brown, L. J. Slutsky, and J. Zaug (1997), The elastic constants of San Carlos olivine to 17 GPa, *J. Geophys. Res.*, *102*, 12,253–12,263, doi:10.1029/97JB00682.

Bai, Q., and D. L. Kohlstedt (1992), High-temperature creep of olivine single-crystals. 2. Dislocation-structures, *Tectonophysics*, *206*, 1–29, doi:10.1016/0040-1951(92)90365-D.

Bai, Q., S. J. Mackwell, and D. L. Kohlstedt (1991), High-temperature creep of olivine: 1. Mechanical results for buffered samples, *J. Geophys. Res.*, *96*, 2441–2463, doi:10.1029/90JB01723.

Ben Ismail, W., and D. Mainprice (1998), An olivine fabric database: An overview of upper mantle fabrics and seismic anisotropy, *Tectonophysics*, *296*, 145–157, doi:10.1016/S0040-1951(98)00141-3.

Béringhier, M., L. Delannay, Y. Chastel, and R. Logé (2007), Using Lagrangian particles to efficiently describe microstructure evolution in metal forming—Application to texture-induced mechanical anisotropy, *Model. Simul. Mater. Sci. Eng.*, *15*, 191–204, doi:10.1088/0965-0393/15/3/001.

Blackman, D. K., J. A. Orcutt, D. W. Forsyth, and J. M. Kendall (1993), Seismic anisotropy in the mantle beneath an oceanic spreading center, *Nature*, *366*, 675–677, doi:10.1038/366675a0.

Brezzi, F., and M. Fortin (1991), *Mixed and Hybrid Finite Elements Methods*, *Ser. in Comput. Math.*, vol. 15, 350 pp., Springer, New York.

Bunge, H. J. (1992), *Texture Analysis in Materials Sciences*, 593 pp., Butterworths, London.

Bystricky, M., K. Kunze, L. Burlini, and J. P. Burg (2000), High shear strain of olivine aggregates: Rheological and seismic consequences, *Science*, *290*, 1564–1567, doi:10.1126/science.290.5496.1564.

Chastel, Y. B., P. R. Dawson, H. R. Wenk, and K. Bennett (1993), Anisotropic convection with implications for the upper-mantle, *J. Geophys. Res.*, *98*, 17,757–17,771, doi:10.1029/93JB01161.

Chenot, J. L., and F. Bay (1998), An overview of numerical modelling techniques, *J. Mater. Processes Technol.*, *80–81*, 8–15, doi:10.1016/S0924-0136(98)00205-2.

Christensen, U. R. (1987), Some geodynamical effects of anisotropic viscosity, *Geophys. J. R. Astron. Soc.*, *91*, 711–736.

Couvy, H., D. J. Frost, F. Heidelbach, K. Nyilas, T. Ungar, S. Mackwell, and P. Cordier (2004), Shear deformation experiments of forsterite at 11GPa-1400 degrees C in the multianvil apparatus, *Eur. J. Mineral.*, *16*, 877–889, doi:10.1127/0935-1221/2004/0016-0877.

Darot, M., and Y. Gueguen (1981), High-temperature creep of forsterite single-crystals, *J. Geophys. Res.*, *86*, 6219–6234, doi:10.1029/JB086iB07p06219.

Dawson, P. R., S. R. MacEwen, and P. D. Wu (2003), Advances in sheet metal forming analyses: Dealing with mechanical anisotropy from crystallographic texture, *Int. Mater. Rev.*, *48*, 86–122, doi:10.1179/095066003225002415.

Doukhan, N., J. C. Doukhan, J. D. FitzGerald, P. N. Chopra, and M. S. Paterson (1984), A TEM microstructural study of experimentally deformed Anita Bay dunite, in *Deformation of Ceramics II*, edited by R. E. Tressler and R. C. Bradt, pp. 307–319, Plenum, New York.

Durham, W. B., and C. Goetze (1977), Plastic flow of oriented single-crystals of olivine: 1. Mechanical data, *J. Geophys. Res.*, *82*, 5737–5753, doi:10.1029/JB082i036p05737.

Durham, W. B., C. Goetze, and B. Blake (1977), Plastic flow of oriented single-crystals of olivine: 2. Observations and interpretation of the dislocation structures, *J. Geophys. Res.*, *82*, 5755–5770, doi:10.1029/JB082i036p05755.

Eshelby, J. (1957), The determination of the elastic field of an ellipsoidal inclusion, and related problems, *Proc. R. Soc. London, Ser. A*, *241*, 376–396, doi:10.1098/rspa.1957.0133.

Gillet-Chaulet, F., O. Gagliardini, J. Meyssonnier, M. Montagnat, and O. Castelnau (2005), A user-friendly anisotropic flow law for ice-sheet modelling, *J. Glaciol.*, *51*, 3–14, doi:10.3189/172756505781829584.

Goetze, C., and D. L. Kohlstedt (1973), Laboratory study of dislocation climb and diffusion in olivine, *J. Geophys. Res.*, *78*, 5961–5971, doi:10.1029/JB078i026p05961.

Hill, R. (1948), A theory of the yielding and plastic flow of anisotropic metals, *Proc. R. Soc. London*, *193*, 281–297, doi:10.1098/rspa.1948.0045.

Honda, S. (1986), Strong anisotropic flow in a finely layered asthenosphere, *Geophys. Res. Lett.*, *13*, 1454–1457, doi:10.1029/GL013i013p01454.

Jung, H., I. Katayama, Z. Jiang, I. Hiraga, and S. Karato (2006), Effect of water and stress on the lattice-preferred orientation of olivine, *Tectonophysics*, *421*, 1–22, doi:10.1016/j.tecto.2006.02.011.

Kaminski, E., and N. M. Ribe (2001), A kinematic model for recrystallization and texture development in olivine polycrystals, *Earth Planet. Sci. Lett.*, *189*, 253–267, doi:10.1016/S0012-821X(01)00356-9.

Kaminski, E., and N. M. Ribe (2002), Timescales for the evolution of seismic anisotropy in mantle flow, *Geochem. Geophys. Geosyst.*, *3*(8), 1051, doi:10.1029/2001GC000222.

Kim, D., F. Barlat, S. Bouvier, M. Rabahallah, T. Balan, and K. Chung (2007), Non-quadratic anisotropic potentials based on linear transformation of plastic strain rate, *Int. J. Plast.*, *23*, 1380–1399, doi:10.1016/j.ijplas.2007.01.006.

Lebensohn, R. A., and C. N. Tomé (1993), A self-consistent anisotropic approach for the simulation of plastic deformation and texture development of polycrystals: Application to zirconion alloys, *Acta Metall. Mater.*, *41*, 2611–2624, doi:10.1016/0956-7151(93)90130-K.

Le Roux, V., A. Tommasi, and A. Vauchez (2008), Feedback between melt percolation and deformation in an exhumed lithosphere-asthenosphere boundary, *Earth Planet. Sci. Lett.*, *274*, 401–413, doi:10.1016/j.epsl.2008.07.053.

Lev, E., and B. H. Hager (2008), Rayleigh-Taylor instabilities with anisotropic lithospheric viscosity, *Geophys. J. Int.*, *173*, 806–814, doi:10.1111/j.1365-246X.2008.03731.x.

Logé, R. E., and Y. B. Chastel (2006), Coupling the thermal and mechanical fields to metallurgical evolutions within a finite element description of a forming process, *Comput. Methods Appl. Mech. Eng.*, *195*, 6843–6857, doi:10.1016/j.cma.2004.11.034.

Mackwell, S. J., D. L. Kohlstedt, and M. S. Paterson (1985), The role of water in the deformation of olivine single-crystals, *J. Geophys. Res.*, *90*, 11,319–11,333, doi:10.1029/JB090iB13p11319.

Mainprice, D., A. Tommasi, H. Couvy, P. Cordier, and D. J. Frost (2005), Pressure sensitivity of olivine slip systems and seismic anisotropy of Earth's upper mantle, *Nature*, *433*, 731–733, doi:10.1038/nature03266.

Montagner, J. P. (1998), Where can seismic anisotropy be detected in the Earth's mantle? In boundary layers. . ., *Pure Appl. Geophys.*, *151*, 223–256, doi:10.1007/s000240050113.

Montagner, J. P., and H. C. Nataf (1986), A simple method for inverting the azimuthal anisotropy of surface waves, *J. Geophys. Res.*, *91*, 511–520, doi:10.1029/JB091iB01p00511.

Muhlhaus, H. B., L. Moresi, and M. Cada (2004), Emergent anisotropy and flow alignment in viscous rock, *Pure Appl. Geophys.*, *161*, 2451–2463, doi:10.1007/s00024-004-2575-5.

Ning, J., and E. C. Aifantis (1996), Anisotropic yield and plastic flow of polycrystalline solids, *Int. J. Plast.*, *12*, 1221–1240, doi:10.1016/S0749-6419(98)80003-X.

Phakey, P., G. Dollinger, and J. Christie (1972), Transmission electron microscopy of experimentally deformed olivine crystals, in *Flow and Fracture of Rocks*, *Geophys. Monogr. Ser.*, vol. 17, edited by H. C. Heard et al., pp. 117–138, AGU, Washington, D. C.

Pouilloux, L., E. Kaminski, and S. Labrosse (2007), Anisotropic rheology of a cubic medium and implications for geological materials, *Geophys. J. Int.*, *170*, 876–885, doi:10.1111/j.1365-246X.2007.03461.x.

Powell, C. M. A., S. R. Roots, and J. J. Veewers (1988), Pre-breakup continental extension in East Gondwanaland and the early opening of the eastern Indian Ocean, *Tectonophysics*, *155*, 261–283, doi:10.1016/0040-1951(88)90269-7.

Raabe, D., P. Klose, B. Engl, K. P. Imlau, F. Friedel, and F. Roters (2002), Concepts for integrating plastic anisotropy into metal forming simulations, *Adv. Eng. Mater.*, *4*, 169–180, doi:10.1002/1527-2648(200204)4:4<169::AID-ADEM169>3.0.CO;2-G.

Raleigh, C. B. (1968), Mechanisms of plastic deformation of olivine, *J. Geophys. Res.*, *73*, 5391–5407, doi:10.1029/JB073i016p05391.

Raterron, P., J. Chen, L. Li, D. Weidner, and P. Cordier (2007), Pressure-induced slip-system transition in forsterite: Single-crystal rheological properties at mantle pressure and temperature, *Am. Mineral.*, *92*, 1436–1445, doi:10.2138/am.2007.2474.

Ribe, N. M. (1989), Seismic anisotropy and mantle flow, *J. Geophys. Res.*, *94*, 4213–4223, doi:10.1029/JB094iB04p04213.

Richter, F. M., and S. F. Daly (1978), Convection models having a multiplicity of large horizontal scales, *J. Geophys. Res.*, *83*, 4951–4956, doi:10.1029/JB083iB10p04951.

Sachs, G. (1928), Zur Ableitung einer Fließbedingung, *Z. Ver. Dtsch. Ing.*, *72*, 734–736.

Schumacher, M. E. (2002), Upper Rhine Graben: Role of preexisting structures during rift evolution, *Tectonics*, *21*(1), 1006, doi:10.1029/2001TC900022.

Silver, P. G., and W. W. Chan (1986), Observations of body wave multipathing from broad-band seismograms: Evidence for lower mantle slab penetration beneath the Sea of Okhotsk, *J. Geophys. Res.*, *91*, 13,787–13,802, doi:10.1029/JB091iB14p13787.

Taylor, G. I. (1938), Plastic strain in metals, *J. Inst. Met.*, *62*, 307–324.

Theunissen, K., J. Klerkx, A. Melnikov, and A. Mruma (1996), Mechanisms of inheritance of rift faulting in the western branch of the East African Rift, Tanzania, *Tectonics*, *15*, 776–790, doi:10.1029/95TC03685.

Tommasi, A. (1998), Forward modeling of the development of seismic anisotropy in the upper mantle, *Earth Planet. Sci. Lett.*, *160*, 1–13, doi:10.1016/S0012-821X(98)00081-8.

Tommasi, A., and A. Vauchez (2001), Continental rifting parallel to ancient collisional belts: An effect of the mechanical anisotropy of the lithospheric mantle, *Earth Planet. Sci. Lett.*, *185*, 199–210, doi:10.1016/S0012-821X(00)00350-2.

Tommasi, A., B. Tikoff, and A. Vauchez (1999), Upper mantle tectonics: Three-dimensional deformation, olivine crystallographic fabrics and seismic properties, *Earth Planet. Sci. Lett.*, *168*, 173–186, doi:10.1016/S0012-821X(99)00046-1.

Tommasi, A., D. Mainprice, G. Canova, and Y. Chastel (2000), Viscoplastic self-consistent and equilibrium-based modeling of olivine lattice preferred orientations: Implications for the upper mantle seismic anisotropy, *J. Geophys. Res.*, *105*, 7893–7908, doi:10.1029/1999JB900411.

Tommasi, A., M. Godard, G. Coromina, J. M. Dautria, and H. Barsczus (2004), Seismic anisotropy and compositionally induced velocity anomalies in the lithosphere above mantle plumes: A petrological and microstructural study of mantle xenoliths from French Polynesia, *Earth Planet. Sci. Lett.*, *227*, 539–556, doi:10.1016/j.epsl.2004.09.019.

Tommasi, A., A. Vauchez, and D. A. Ionov (2008), Deformation, static recrystallization, and reactive melt transport in shallow subcontinental mantle xenoliths (Tok Cenozoic volcanic field, SE Siberia), *Earth Planet. Sci. Lett.*, *272*, 65–77, doi:10.1016/j.epsl.2008.04.020.

Tucker, G. E. G. (1961), Texture and earing in deep drawing of aluminium, *Acta Metall.*, *9*, 275–286, doi:10.1016/0001-6160(61)90220-6.

Vauchez, A., A. Tommasi, and G. Barruol (1998), Rheological heterogeneity, mechanical anisotropy and deformation of the continental lithosphere, *Tectonophysics*, *296*, 61–86, doi:10.1016/S0040-1951(98)00137-1.

Vinnik, L., B. Romanowicz, and L. Breger (1994), Anisotropy in the center of the Inner-Core, *Geophys. Res. Lett.*, *21*, 1671–1674, doi:10.1029/94GL01600.

Von Mises, R. (1913), Mechanik der festen Korper in plastich-deformablen Zustand, *Nachr. Ges. Wiss. Goettingen, Math. Phys. Kl.*, *1*, 582–592.

Wenk, H. R., K. Bennett, G. R. Canova, and A. Molinari (1991), Modeling plastic-deformation of peridotite with self-consistent theory, *J. Geophys. Res.*, *96*, 8337–8349, doi:10.1029/91JB00117.

Zhang, S. Q., and S. Karato (1995), Lattice preferred orientation of olivine aggregates deformed in simple shear, *Nature*, *375*, 774–777, doi:10.1038/375774a0.

Zhao, Z., F. Roters, W. Moo, and D. Raabe (2001), Introduction of a texture component crystal plasticity finite element method for anisotropy simulations, *Adv. Eng. Mater.*, *3*, 984–990, doi:10.1002/1527-2648(200112)3:12<984::AID-ADEM984>3.0.CO;2-L.